



RESEARCH ARTICLE

10.1002/2017JC012708

On the dynamics of flow past a cylinder: Implications for CTD package motions and measurements

D. R. Munday¹ and M. P. Meredith¹ ¹British Antarctic Survey, Cambridge, UK

Key Points:

- CTD measurements are known to suffer from wake effects caused by the package descent through the water column
- A simple 2-D model of flow past a cylinder reveals the sensor locations that are comparatively most and least affected by this process
- Oscillation of the flow, simulating heave, indicates that long-period oscillations are less damaging to data quality than short-period ones

Supporting Information:

- Supporting Information S1
- Movie S1
- Movie S2
- Movie S3
- Movie S4
- Movie S5
- Movie S6
- Movie S7
- Movie S8
- Movie S9

Correspondence to:

D. R. Munday,
danday@bas.ac.uk

Citation:

Munday, D. R., and M. P. Meredith (2017), On the dynamics of flow past a cylinder: Implications for CTD package motions and measurements, *J. Geophys. Res. Oceans*, 122, 5708–5728, doi:10.1002/2017JC012708.

Received 24 JAN 2017

Accepted 12 MAY 2017

Accepted article online 22 MAY 2017

Published online 17 JUL 2017

© 2017. The Authors.

This is an open access article under the terms of the Creative Commons Attribution License, which permits use, distribution and reproduction in any medium, provided the original work is properly cited.

Abstract During the collection of ship-based observations, heaving of the vessel may lead to variation in the descent rate of a CTD package. This can result in the package being pulled upward through previously sampled water, leading to difficult to quantify errors due to the complex wake. To reduce this problem to one of manageable stature, we use the simple paradigm of two-dimensional flow past a cylinder. By using a tracer with a gradient along the flow, we quantify the effect of the cylinder on its distribution and the impact of postprocessing. At high Reynolds numbers, over 200, uniform translation leads to a small error in the tracer value. This error is likely negligible at the much higher Reynolds number of the ocean. When the flow is oscillated longitudinally, there are two main sources of error; attached vortices may propagate around the cylinder and/or shed vortices may translate into the path of the cylinder. Postprocessing by removing records from previous pressure levels removes much of the first error, due to it occurring as the package ascends. However, the second source of error is more difficult to remove, due to it occurring when the package is once again descending. In general, results indicate that long-period oscillations are preferable. While the magnitude of the errors are comparable to those from short-period oscillations, they are spread farther apart in time and space and the overall effect is to localize the errors in small regions of the final depth profile.

1. Introduction

Conductivity-Temperature-Depth (CTD) instruments are the workhorses of ship-based oceanography. For measuring below the surface layer of the ocean, CTDs are commonly mounted on frames that are lowered and raised on conducting cables, with data transmission through the cable to a deck unit on the research vessel. Such instruments can sample ocean properties at high frequencies (typically 24 Hz) and with high precisions (targets of 0.002°C for temperature, 0.002 for salinity, 2dbar for pressure), enabling reliable derivation of properties in vertically averaged intervals.

Other sensors and equipment are often deployed on the CTD frame, including arrays of Niskin bottle samplers, altimeters and pingers that enable controlled near-seabed approach, acoustic Doppler current profilers, and so on. The ability to interact with the CTD package in real-time from the ship allows control of how and when sampling is conducted, e.g., the temporary halting of the package at a target level in the ocean and the closing of Niskin bottles to collect discrete samples.

It has long been understood that the CTD package is not an independent sampler of the environment in which it sits, and that its presence and behavior in the water can affect the data that are recovered. One example of this is the warming of seawater by the CTD conductivity cell; if this same water is then passed over a temperature sensor (as commonly occurs in modern pumped CTD systems), a cell thermal mass effect is generated that must be corrected for in order to obtain the highest precision data [Lueck and Picklo, 1990]. Algorithms to achieve this are well established.

Another example of the CTD package influencing the environment that it samples derives from the motion of the package itself. Typically, packages are lowered and raised at around 1 ms⁻¹ for deep ocean casts (though at lower speeds nearer the surface and the seabed), with a continuous downcast conducted and the package stopped at intervals during the upcast to collect water samples. Data from the downcast are generally prioritized for use in scientific analyses, and hence the CTD sensors are normally fixed near the bottom of the frame so that they encounter water before the rest of the frame and equipment mounted thereon. In theory, this provides the “cleanest” data on the downcast, whereas upcast CTD data are

potentially more influenced by the effects of the package. When collecting water samples on the upcast, it is common practice to park the package at the desired sampling level and allow water so influenced to disperse before closing a Niskin, the hope by doing so being to minimize these effects, and hence to maximize the compatibility of the CTD data and discrete sample collected.

While the downcast of a CTD profile can be less impacted by package effects than the upcast, it is known to not be immune [e.g., *Trump*, 1983; *Aijun*, 1991, and references therein]. The downward motion of the package inevitably induces a response in the seawater through which it transits, and can lead to the existence of a wake in its lee. Of particular note is that variations in CTD vertical speed, such as are associated with the ship rolling, can have significant impact on the quality of the data being collected. In essence, if the package's motion through the water on a downcast slows, the water trapped in the wake behind it can slump downward around the package onto the CTD sensors. This can result in their measurement of water from a potentially higher level in the ocean than the one at which the package sits. In extreme cases, a reversal of the CTD downward motion can pull the package upward through depths in the ocean that it has already encountered. Such effects can lead to pronounced perturbations in the data collected, especially in regions of strong vertical gradients in ocean properties [*Trump*, 1983].

Time-varying package speed is almost inevitable, and while its impact may often be small (e.g., in calm seas), ship roll in rougher sea states can lead to significant degradation of data quality. Data collected that are affected are often still useful for determining bulk water mass characteristics, deriving (baroclinic) geostrophic flows, and so on, but are compromised for investigations of ocean fine structure and related processes.

Data processing techniques exist for minimizing the impact of ship roll effects and CTD wakes on data quality. Typically these include the imposition of data exclusion for periods when the package velocity was too low (e.g., less than 0.3 ms^{-1} on a downcast), and/or sections of data from depth levels shallower than ones already encountered (which would denote the package having been raised by a ship roll before recommencing its downward motion). These criteria can be varied and other methods adopted (e.g., manual removal of data sections) so as to optimize the quality of the data retained, however there is no perfect data processing solution for this. Even if all the data influenced by wakes could be identified and removed, and only data independent of wakes retained in the final profiles, this still means fewer data being used to construct those profiles than the instruments are optimally capable of delivering.

There have been various engineering and mechanical attempts to help alleviate this issue. These include the development of compensating winch systems; however, these are still not commonplace on research vessels. The fixing of CTD sensors away from the main body of the package (e.g., on a horizontal arm or fin) has also been attempted, and while there is merit in this approach, there is also a need to better understand the nature of the flow distortion created by the package if the data are to be correctly interpreted, and the optimal positioning/distance to be established. There is thus a need to understand more fully the dynamical interaction of a CTD package with the water through which it moves, in order to better comprehend the likely impact on data under different ocean conditions and different characteristics of package motion.

To illustrate the problem of CTD package motion influencing the data collected, Figure 1 shows a segment of CTD data from a profile conducted in the Scotia Sea region of the Southern Ocean during a period of particularly heavy swell. The rolling of the ship induced by the swell is clearly visible in the pressure recorded by the CTD package (Figure 1a), with frequent instances of declining pressure present as the package's descent was stalled and reversed. In the profile of density calculated from the same section of CTD data (Figure 1b), it can be seen that these rolls were manifested as sections of data with little vertical density change (or even apparent declines in density with depth), interspersed with sudden, unrealistic increases in density. In both plots, the green points indicate the data remaining after a standard automated routine has been applied with the intention of removing points obviously influenced by these effects; this routine excludes data collected during periods in which the CTD package's downward descent was less than 0.24 ms^{-1} . It can be seen that this routine identifies well the sections of data during which package was slowed or reversed by the ship's rolls (Figure 1a), but that the property data itself (Figure 1b) was so influenced by the CTD motion effects at all times that the remaining data are still heavily contaminated. In essence, the whole section of data is significantly influenced by the CTD motion effects, and choices concerning the automated exclusion of data become simple selections of how to subsample that contaminated data.

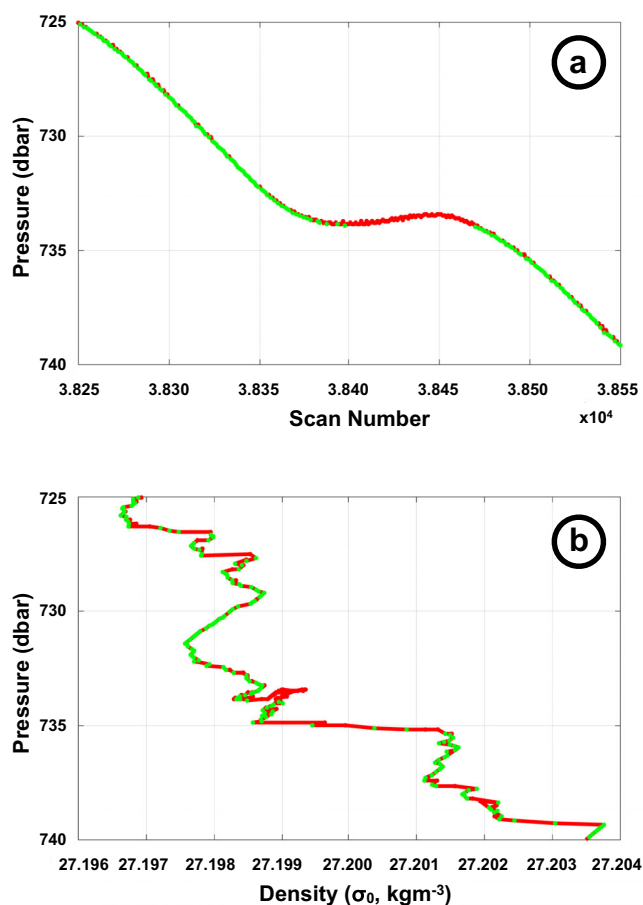


Figure 1. (a) Pressure data collected from a CTD profile conducted in the Scotia Sea during a period of heavy swell. Red line denotes CTD pressure collected at a scan rate of 24 Hz. Green line denotes the same data, with periods during which the CTD package's downward descent was less than 0.24 m/s excluded. (b) Same as top plot but for calculated density rather than scan number. Note that the automated processing to remove data points based on the package motion does a good job of identifying the periods of slow or reversed descent (a), but that even when data from these periods are excluded, the remaining data are still heavily influenced by the effects of the CTD motion (b).

A well-known paradigm of the wakes that form behind bluff bodies and flow separation is flow past a cylinder. While this is a major simplification of a CTD package's complex and permeable 3-D manifold, it is a problem with many engineering applications and a wealth of literature is therefore available. This literature includes detailed investigation of the physics that occur when the flow is oscillating instead of uniformly translating, as well as the combination of a constant flow component with transverse and longitudinal oscillations of that flow. These can be taken as analogues of the CTD package swinging on the winch cable (transverse oscillation) or ship roll pulling the package back through the water column (longitudinal oscillation). By beginning with such a well-studied and understood example, a solid foundation is laid for deeper understanding of how a CTD package's wake may affect the measurements taken by its sensors. Furthermore, to model the full complexity of a CTD package would require large HPC resources. By starting with a simple test case of a 2-D cylinder, we are able to draw useful conclusions with a small computing effort. Important differences between the 2-D and 3-D cases will no doubt occur. However, the 2-D case is an extremely well-documented and understood starting point.

This paper is organized as follows. Section 2 reviews the dynamics of flow past a cylinder, including the effects of flow oscillation. Section 3 describes the numerical model and domain used to conduct the flow past a cylinder experiments. Section 4 addresses how the presence of a cylinder, and its wake, in a uniform flow may alter the transport of a passive tracer through the domain. Section 5 applies the same approach to the case of sinusoidally oscillating flow without net translation. Section 6 combines the uniform flow with a longitudinal oscillation to simulate how heaving of a ship may alter the measurements taken by a CTD mounted on a frame. We close with a summary and discussion of our results in section 7.

2. Flow Past A Cylinder

The simple case of uniform flow past a stationary cylinder is controlled by a single parameter; the *Reynolds number*, given by

$$\text{Re} = \frac{U_0 L}{\nu}, \quad (1)$$

where U_0 is the velocity of the flow, L is the cylinder diameter, and ν is the kinematic viscosity. This is deceptively simple and a range of flow regimes, including the transition to turbulence, results from variation in

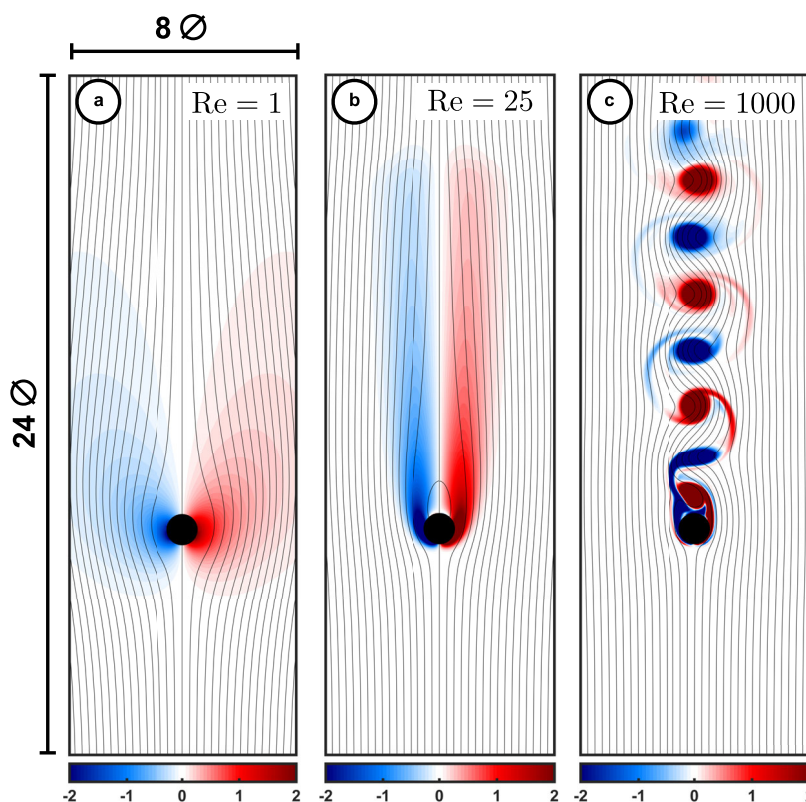


Figure 2. Numerical solutions for uniform flow past a cylinder at the Reynolds number shown. Relative vorticity is shown in color with stream function as black contours 0.25 nondimensional units apart. Only part of the model domain is shown, see section 3 for full details of the numerical approach.

Re. Excellent example images of the different regimes can be found in *Van Dyke* [1982] and are illustrated in Figure 2 (see section 3, below, for details of how the numerical results of Figure 2 were produced).

As the Reynolds number increases, the flow past a cylinder transitions from fully attached flow with near-symmetry in the along-flow direction ($Re < 1$, Figure 2a) to laminar separation with a pair of attached vortices behind the cylinder ($10 < Re < 40$, Figure 2b). At higher Re , the wake itself becomes unstable and can wrap up into a von Kármán vortex street, producing an unsteady flow despite the steady boundary conditions. As shown in Figure 2c, a vortex street consists of pairs of vortices of alternate sense of rotation being shed from the cylinder. As the Reynolds number continues to increase, this vortex street persists until the wake becomes fully turbulent at $Re > 1000$. However, patterns akin to vortex streets remain in the flow even at the extremely high Reynolds numbers ($\sim 10^6 - 10^7$) found in, e.g., atmospheric and oceanic flows, such as the leaking crude oil behind the tanker *Argo Merchant* in plate 173 of *Van Dyke* [1982].

When the flow past a cylinder is sinusoidally oscillated, instead of uniformly translated, a second parameter is introduced; the *Keulegan-Carpenter number*, KC , named for *Keulegan and Carpenter* [1958]. The Keulegan-Carpenter number describes the relative length of the oscillation period and the advective timescale (L/U_0) and is given by

$$KC = \frac{U_0 T}{L}, \quad (2)$$

where U_0 is now the maximum flow velocity, i.e., the amplitude of the velocity oscillation, and T is the period of the oscillation. KC can be interpreted as the nondimensional period of the flow oscillation.

As KC is varied a wide range of flow regimes results [*Tatsuno and Bearman*, 1990; *Dütsch et al.*, 1998], with the regime achieved only weakly dependent upon Re . As summarized by *Lam and Dai* [2002], for low values of KC the flow is symmetric around the cylinder, and symmetric vortex shedding, where opposite signs of vortex are next to each other, may occur. In the range $4 < KC < 8$ asymmetric vortex shedding, where

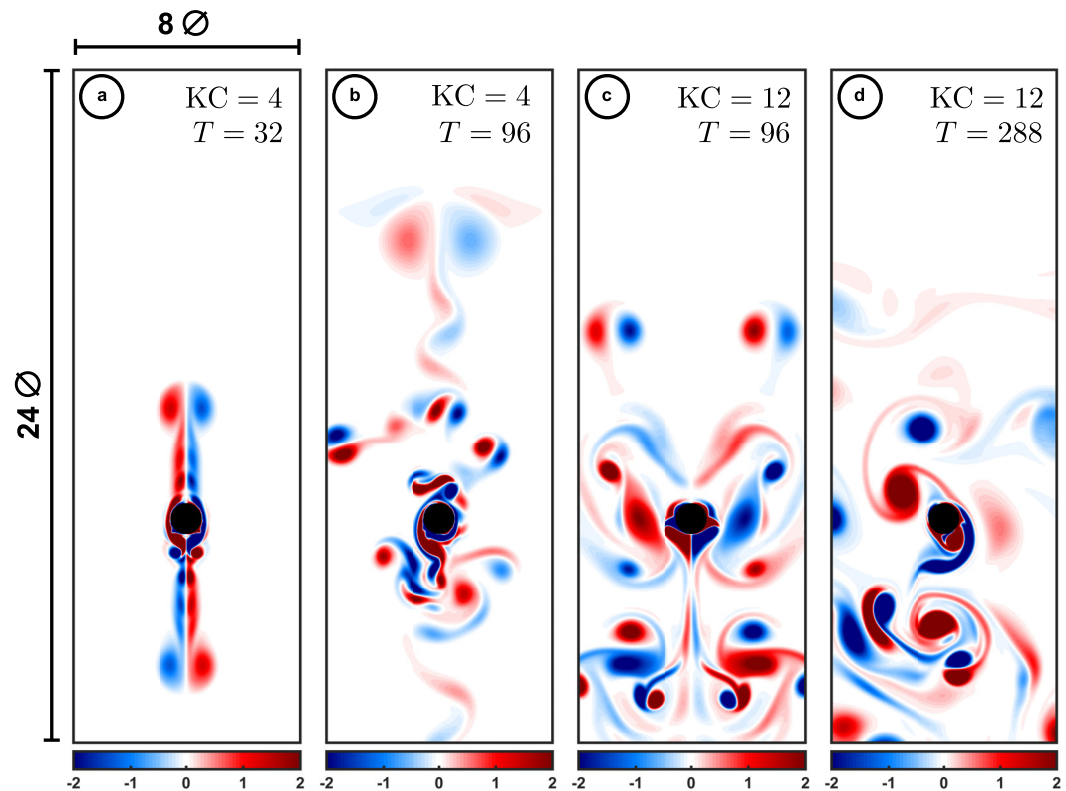


Figure 3. Numerical solutions for oscillating flow past a cylinder at the Keulegan-Carpenter number and nondimensional time, T , shown for $Re=1000$. Each frame corresponds to the end of a full cycle and the externally imposed flow is currently at rest, hence only relative vorticity is shown in color. Only part of the model domain is shown, see section 3 for full details of the numerical approach.

opposite signs of vortex are staggered longitudinally, takes place and for $KC > 8$ a vortex street transverse to the direction of the oscillation may form. Finally, when $KC > 15$, vortex pairs, or groups, form within the flow.

The complex interactions of the resulting vortices that can result are illustrated in Figures 3a and 3b, for $KC=4$, and Figures 3c and 3d for $KC=12$. A Reynolds number of 1000 was used for these two simulations. Initially, both numerical solutions are left-right symmetric, as is the vortex shedding, as shown by Figures 3a and 3c, which are both eight oscillation periods after model initialization. For $KC=4$, the vortices formed on each side of the cylinder during a half-cycle translate to, and are shed from, the opposite side of the cylinder as the flow reverses. There they merge with vortices from previous half cycles into a single vortex pair. As shown in Figure 3b, these large vortex pairs propagate away from the cylinder (Figure 3c) with the breaking of left-right symmetry in the flow cutting off their supply of vorticity and leading to their eventual dissipation. The breaking of this symmetry also leads to the development of a more complex flow with small, intense vortex pairs being shed on each half cycle.

At $KC=12$, the vortices that form in one half cycle are still shed from the opposite side of the cylinder. However, they do not merge into a single vortex and instead remain free to propagate around the domain and may interact or merge with any of the other vortices that are present. Once the left-right symmetry in the domain breaks, a vortex may shed from the side of the cylinder it formed on, prior to the reversal of the flow, and short von Kármán vortex streets may result. The vortex interactions become increasingly complex. Animations of all the numerical solutions summarized in Figures 2 and 3 are available as supporting information. These animations portray the beautiful and complex nature of the vortex interactions that may result from a deceptively simple example of flow past a cylinder far better than the snapshots of the flow shown here.

A second definition of the Keulegan-Carpenter number is also available for situations in which the position of the cylinder is oscillated, rather than the incident flow. In these circumstances, KC can be written as

$$KC = \frac{2\pi A}{L}, \tag{3}$$

where A is the amplitude of the cylinder motion. This definition is equivalent to that given in equation (2), highlighting the dynamical similarity between periodic fluctuations of the flow past a cylinder and moving the cylinder through an otherwise quiescent fluid. The connection is easy to see by assuming the flow evolves according to $U_0 \sin(2\pi t/T)$ and solving for the resulting displacement, giving $A = U_0 T / 2\pi$.

The ratio of Reynolds number and the Keulegan-Carpenter number is known as the frequency parameter [Sarpkaya, 2005] and is given by

$$\beta = \frac{Re}{KC} = \frac{L^2}{\nu T}. \tag{4}$$

Although there are three nondimensional parameters that define the flow, only two are independent. Here we choose to specify Re and KC and use a large value of Re to ensure weak dependence of the flow upon its value [Lam and Dai, 2002]. Typically the sensitivity to Re and/or β is found to be small at sufficiently high values.

Of particular relevance to the sampling issues surrounding CTD package is the combination of uniform translation with a transverse or longitudinal oscillation of the flow. While swinging of the package may lead to transverse variations as the package descends, it is far more likely that rolling of the ship will lead to changes in the descent rate, i.e., longitudinal oscillation of the flow. In this case, the in-flow toward a stationary cylinder can be approximated as

$$U = U_0 + \Delta U \sin\left(\frac{2\pi t}{T}\right), \tag{5}$$

where U is the inflow velocity, U_0 is the constant component of the inflow, and ΔU is the amplitude of the velocity oscillation.

Combining a uniform flow with an oscillating component introduces an additional parameter that can influence the flow. The first two parameters are as before; the Reynolds number and the Keulegan-Carpenter number (usually called the *reduced velocity* in these circumstances, e.g., Konstantinidis and Balabani, 2007). The third parameter is the *reduced amplitude*, given by

$$A^* = \frac{\Delta U T}{2\pi L} = \frac{1}{2\pi} \frac{\Delta U}{U_0} KC. \tag{6}$$

A^* is the nondimensional displacement of the cylinder, if its motion provides the oscillatory part of the flow, or a fluid parcel if the incident flow is oscillated. It clearly breaks the equivalence between the two definitions of KC given in equations (2) and (3). A^* reflects that the magnitude of the velocity oscillation, as well as the period of the oscillation, determines how far the cylinder/fluid parcel moves during a full cycle. For larger values of A^* and KC , the displacement is larger, while at the same value of KC the displacement becomes larger as ΔU increases. For simplicity, we choose to specify the ratio $\Delta U/U_0$ as our third parameter.

Adding longitudinal oscillation of the flow past a cylinder produces a range of interesting flow phenomena. Vortex shedding, and their subsequent interactions, leads to complex wake formations even prior to the breaking of left-right symmetry, as shown in Figure 4 for $KC=4$ and a range of $\Delta U/U_0$ values. These solutions can be compared with Figure 3 of Al-Jamal and Dalton [2013], taking into account that Al-Jamal and Dalton [2013] define the relative strength of the oscillation and mean flow in a reciprocal manner to us (i.e., $\Delta U/U_0 = 1/B$ in Al-Jamal and Dalton [2013]). As with a purely oscillatory flow, vortices may form on one side of the cylinder and shed from the other, with the distance that the vortex is “thrown” depending on both KC and A^* .

Both symmetric and asymmetric modes of vortex shedding have been observed in cylinder flows with longitudinal flow oscillation [Konstantinidis and Balabani, 2007; Al-Jamal and Dalton, 2013]. An example of a symmetric mode is Figure 4c, where the oscillation is sufficiently strong to bring the flow to rest on each cycle and which is taken eight full cycles after model initialization. However, in all the numerical simulations we performed, symmetric modes eventually collapse to give an asymmetric mode, such as in Figure 4d, which is 32 full oscillation cycles after 4c. It is this breaking of symmetry that gives rise to some of the more complex flow patterns and, at some parameter combinations, can allow for the shedding of short von Kármán vortex streets on each half-cycle.

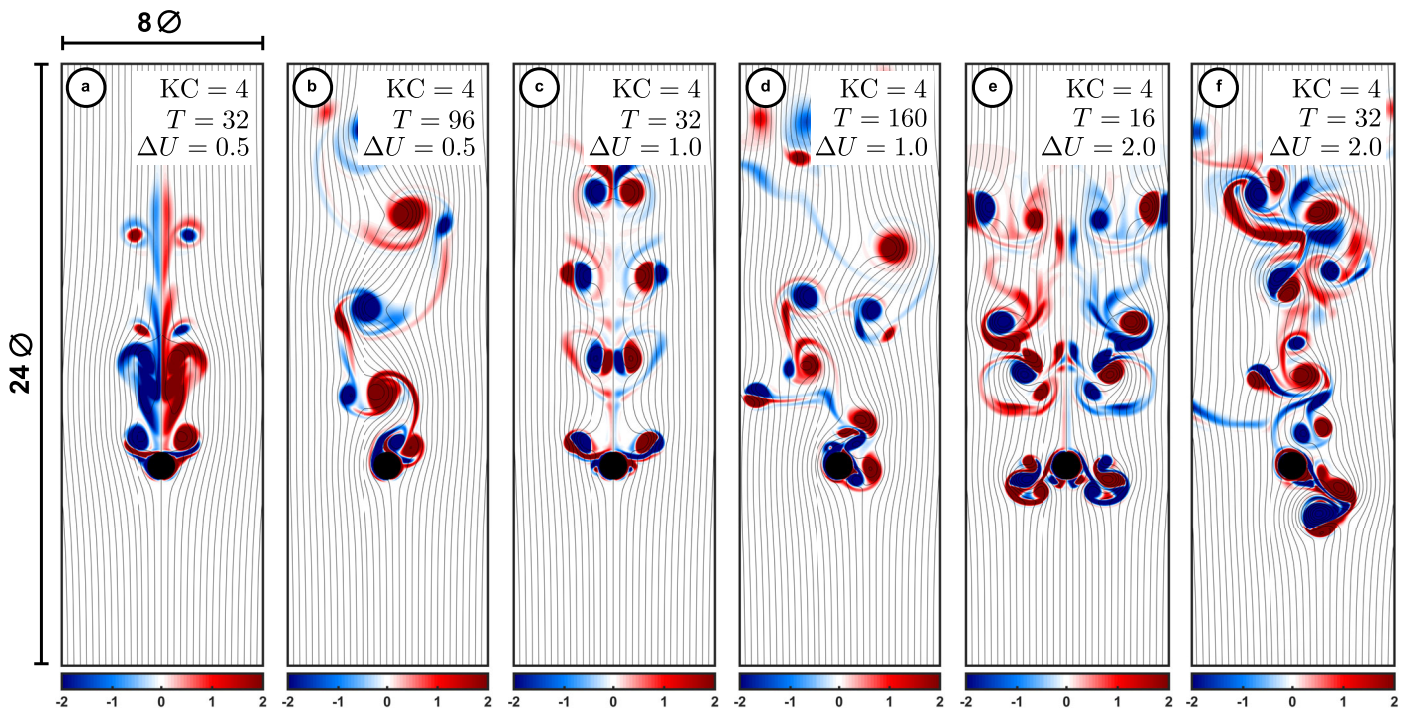


Figure 4. Numerical solutions for oscillating flow past a cylinder at the Keulegan-Carpenter number, nondimensional time, T , and ΔU shown for $Re=1000$. Relative vorticity is shown in color with stream function as black contours 0.25 nondimensional units apart. Each frame corresponds to the end of a full cycle and the externally imposed flow is currently at a magnitude of 1. Only part of the model domain is shown, see section 3 for full details of the numerical approach.

At high Reynolds number, in the range when von Kármán vortex streets are expected, the phenomena of vortex lock-on or lock-in can also occur [Griffin and Hall, 1991; Rao *et al.*, 1992]. This is a form of resonance that occurs when the frequency of the flow oscillation is close to that of the vortex shedding one would expect, i.e., the Strouhal frequency. In this section of parameter space, the frequency of vortex shedding is tied to the Strouhal frequency, rather than the frequency of the flow oscillation, with peaks in the velocity spectra occurring at the Strouhal frequency and its harmonics [Griffin and Hall, 1991]. Note that the Strouhal frequency is only a weak function of Reynolds number.

3. Model Domain and Setup

Since flow past a cylinder, whether constant or oscillating in time, is readily described with just a few nondimensional parameters, we choose to perform our simulations using a nondimensional model. To do so we set the cylinder diameter, L , and the inflow to the domain, U_0 , to 1. Setting Re is then equivalent to setting a nondimensional viscosity. Time is nondimensionalized using the advective timescale, $T=L/U_0$, such that when the inflow oscillates in magnitude KC sets the period of the oscillation. The model domain is 16 cylinder diameters by 32 cylinder diameters with the cylinder itself placed centrally, as shown in Figure 5a. Due to the oscillating flow in some of our experiments, the direction and distance that vortices may travel is unknown a priori, hence the central placement of the cylinder. Within four cylinder diameters of the upper and lower boundary of the domain, sponges are used to relax the flow toward that imposed at the upper and lower boundaries to ensure a smooth entry/exit from the domain and no reflections of vortices from the boundary.

The model solves the 2-D vector-invariant Navier-Stokes equations written in nondimensional form as

$$\frac{\partial \mathbf{u}}{\partial t} + \xi \mathbf{k} \times \mathbf{u} = -\nabla B + \frac{1}{Re} \nabla^2 \mathbf{u} - \frac{1}{R_4} \nabla^4 \mathbf{u} - r_u (\mathbf{u} - \mathbf{U}_0) \quad (7)$$

where $\mathbf{u}=(u, v)$ is the 2-D nondimensional velocity, $\xi=\mathbf{k} \cdot \nabla \times \mathbf{u}$ is the nondimensional vertical vorticity, and $B=p+\mathbf{u} \cdot \mathbf{u}/2$ is the nondimensional Bernoulli potential with p as the nondimensional pressure. r_u is a Newtonian damping coefficient within the sponges and \mathbf{U}_0 is the incoming/outgoing flow at the upper and lower boundaries. At Reynolds numbers in excess of 500, we find that additional biharmonic viscosity of the

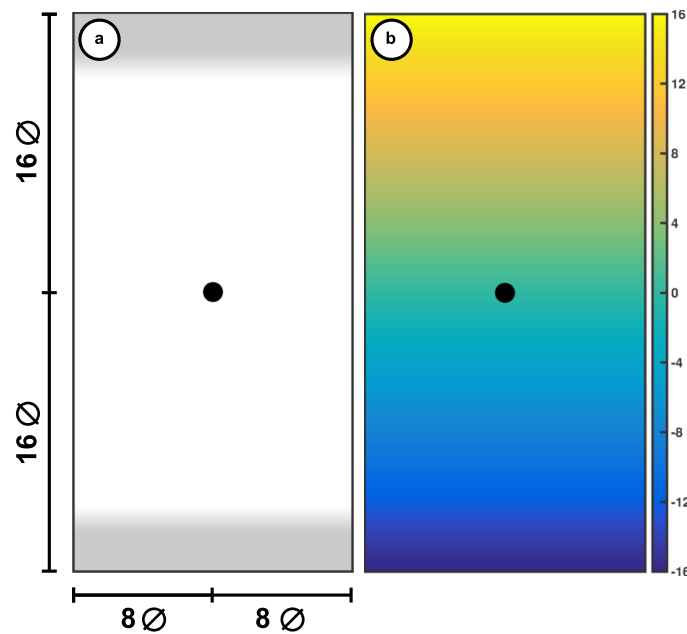


Figure 5. Schematic view of the full model domain with (a) showing the position of the inflow/outflow sponges as grey shading and (b) the initial passive tracer distribution.

form of $R_4 = U_0 L^3 / \nu_4$ (with ν_4 the biharmonic viscosity) is required to maintain numerical stability and prevent noise in the vorticity field. As with *Tansley and Marshall* [2001], we use a value of $R_4 = 3 \times 10^5$ and find at $Re = 200$ that the additional dissipation does not alter the regime of the flow, i.e., a von Kármán vortex street still occurs, and that the flow remains broadly the same.

In order to assess how the wake of a CTD package may affect its own measurements, a passive tracer is added to the flow. Once the flow reaches steady state ($Re < 100$) or statistical equilibrium after the breaking of left-right symmetry ($Re \geq 100$), the tracer is initialized with a value equal to the y coordinate, as per Figure 5b. The tracer is governed by the following equation:

$$\frac{\partial C}{\partial t} + \nabla \cdot (C\mathbf{u}) = \frac{1}{Pe} \nabla^2 C - \frac{1}{P_4} \nabla^4 C - r_C (C - C_0) \quad (8)$$

where Pe is the Péclet number given by $Pe = U_0 L / \kappa_C$, with κ_C being the tracer diffusivity, and P_4 is a biharmonic Péclet number given by $P_4 = U_0 L^2 / \kappa_4$, with κ_4 the biharmonic diffusivity. We use $Pe = 1400$ for all of our experiments and $P_4 = 3 \times 10^6$ when $Re \geq 500$. There is some minor sensitivity to the chosen value of Pe (not shown), although this is not sufficient to alter our conclusions.

The value of the tracer just above and below the cylinder, at $y = \pm 0.571$, is taken as a faux CTD measurement and its difference from what would be obtained by simple translation through the domain by the inflow in the absence of a cylinder. A sponge is also applied to the tracer at the upper and lower boundaries, with the damping coefficient r_C and a profile given by C_0 . This profile is updated to match the translation of the linear gradient through the domain by the inflow, taking account of any periodic oscillations. Combined with the removal of anomalies, this ensures a smooth transition and link between the interior model domain and the rigid boundary condition. In practice, we set $r_C = r_u$ and use the same form and strength of sponge for both momentum and tracer.

The model uses centered second-order differences on a C grid for all terms in the momentum and tracer equations. Lateral boundary conditions are no-slip on the cylinder and free-slip on the left and right walls. We use ghost points to impose these boundary conditions for simplicity. The use of ghost points may lead to spurious form stresses when boundaries are not aligned with the coordinate direction [*Adcroft and Marshall, 1998*]. However, the model shows the expected regimes at a range of Reynolds number, see Figure 2, and the resulting error appears to be small. The nondimensional pressure is solved for using a preconditioned conjugate gradient iterative solver. The tracer equation is prognosticated using a finite volume formulation that conserves its mean value and fluxes of tracer are evaluated using the Superbee flux limiter of *Roe* [1985].

The model domain is discretized on a grid of 512×1024 points. This gives a uniform grid spacing of $L/32$, equivalent to a nondimensional value of 0.03125 and the same as used by *Tansley and Marshall* [2001] over a much smaller domain. At $Re = 1000$, there are $\sim 2-3$ grid points within the boundary layer (defined as the region where the flow speed is < 0.95 at $y = 0.0$) and $\sim 5-6$ grid points prior to the flow speed peaking just outside the viscous boundary layer. Strictly speaking, this is insufficient to properly resolve the laminar

boundary layer that forms at this value of Re . However, further refinement of the model resolution was prohibited by the size of the model domain, the physical memory available and the model run time. This is because the run time of the numerical model varies with the parameters of the system, and the model resolution, due to changes in the number of iterations for convergence of the pressure solver. Typically 32 non-dimensional time units took 2–8 days on a single processor of a linux-based desktop, including the passive tracer. With some experiments requiring in excess of 256 time units to complete, the run time for the entire set of experiments was considerable. Thus the compromise reached between model resolution and the maximum Reynolds number we could attain.

4. Uniform Translation

In this section, we use the passive tracer C to assess the impact of the wake of a cylinder subject to uniform translation on the tracer values just above and below its center line. These experiments are as shown in Figure 2, along with additional experiments carried out at a range of Reynolds numbers between 1 and 2000. We will refer to the upstream side of the cylinder as the downcast side. This reflects that a CTD sensor mounted on the bottom of the rosette would be expected to make measurements on this side.

4.1. Qualitative Description

As described in section 1, and shown in Figure 2, the model's flow patterns are consistent with those expected at the appropriate Reynolds numbers, as are the transitions between regimes. After the model has reached statistical steady state, as measured by the domain average energy becoming constant or any oscillations being of constant amplitude, the passive tracer is added to the domain and the model run continued. The passive tracer's initial condition is as shown in Figure 5b and corresponds to the value being set by the y coordinate. This is then advected past the cylinder with the boundary conditions and sponges enforcing the constant, uniform gradient. Since new values of tracer are continuously introduced at the lower boundary, the tracer value at any location in the domain does not reach a steady state per se. However, the difference between the actual value and that expected for a tracer with a uniform gradient advected by a uniform flow does reach a steady state. As such, after the tracer's introduction, the model run continues until this state is reached.

The final distribution of the difference between the actual tracer value and the expected value is shown for a range of representative Reynolds numbers in Figure 6. Positive values (red colors) indicate the tracer value is more positive than expected, i.e., that during the downcast fluid from higher in the water column has been retained in the wake of the cylinder. Higher values indicate water from higher up the water column.

At a Reynolds number of 1, the flow is left-right symmetric and there is little up-down asymmetry, see Figure 2a. However, the final tracer difference distribution shows that the influence of the cylinder extends upstream, and to the sides, by over a cylinder diameter. On the upcast side of the cylinder, the flow is considerably weaker than the uniform value prescribed at the lower edge of the domain (as seen by the separation between streamlines in Figure 2a) and so the highest values of tracer difference are found here, particularly on the center line of the domain.

At a Reynolds number of 25, the flow retains its left-right symmetry, as shown in Figure 2b, however the cylinder now causes the flow to separate in its wake and generates a pair of counterrotating vortices that do not shed. These vortices are subject to a very weak exchange with the rest of the flow, as indicated by the very high value of tracer difference shown in Figure 6b. While the colorbar in Figure 6b is saturated to allow easy comparison with the other plots, the peak value of tracer difference in the wake is in excess of 90. The boundary layers on the cylinder, and its upstream bow wave, become thinner as the Reynolds number increases, as seen by the lower values to the side and upstream of the cylinder.

In contrast to Reynolds numbers of 1 and 25, at a Reynolds number of 1000, the presence of a von Kármán vortex street on the downstream side of the cylinder prevents the tracer difference from attaining a steady state. Rather, as the cylinder sheds vortices they carry with them fluid that has been retained in its wake. This leads to each vortex containing fluid from higher in the water column and gradually translating away from the cylinder. As with the increase in Reynolds number from 1 to 25, the boundary layers and bow wave of the cylinder are clearly narrower once more.

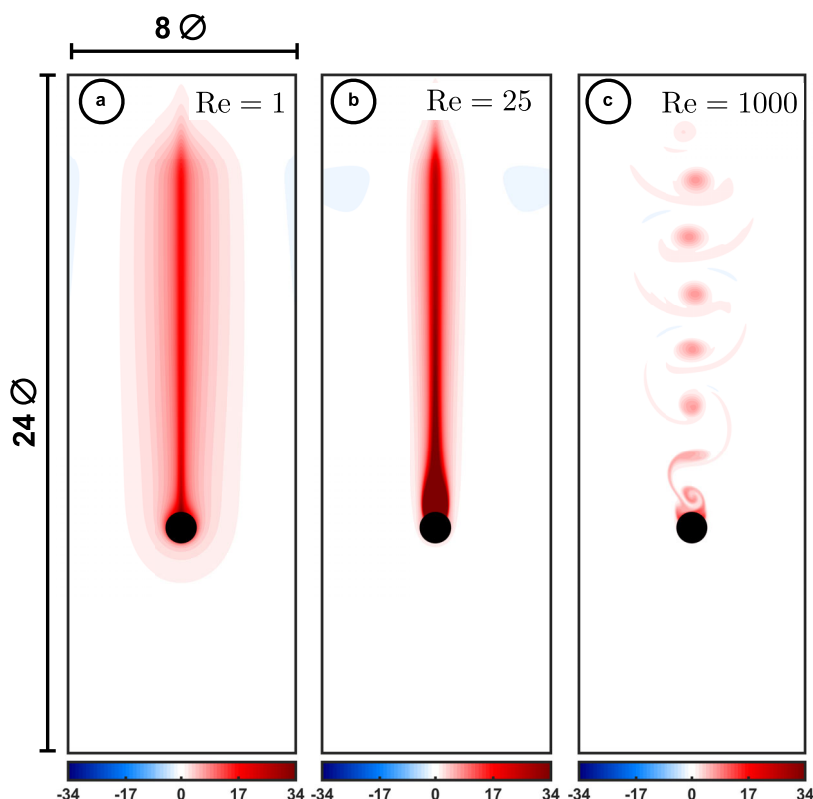


Figure 6. The difference between the actual tracer value and that expected in the absence of the cylinder and its wake at (a) $Re=1$, (b) $Re=25$, and (c) $Re=1000$. Red colors indicate the presence of fluid from higher in the water column, blue colors indicate the presence of fluid from lower in the water column.

4.2. Tracer Variation With Re

The effect of the Reynolds number on the tracer difference can be more quantitatively assessed by considering its variation at a particular point. We select locations on the cylinder's center line and at $y = \pm 0.571$ for the upcast/downcast side. For Reynolds numbers less than 100 or so, these values reach a steady state. At higher Reynolds numbers, this is not the case due to the presence of a von Kármán vortex street. As an example, the variation of time of the upcast and downcast values for the $Re=1000$ case is shown in Figure 7a. There is a very clear oscillation in the tracer difference record on the upcast side of the cylinder.

As vortices form and shed on the upcast side of the cylinder, the domain average kinetic energy undergoes a very low amplitude oscillation ($\sim 0.01\%$ of the long-term time average value). Each peak/trough in the upcast tracer difference corresponds to a peak/trough, with a slight phase difference, in the domain average kinetic energy. At the trough in domain average kinetic energy, the vortex is shed and the next one begins to grow. The growing vortex sequesters tracer from the main flow and so the tracer difference grows until the vortex sheds and the boundary is flushed through with "clean" fluid.

The variation of time-average tracer difference on the downcast side of the cylinder, in Figure 7b, shows a very rapid decrease with Re . By $Re \approx 200$ the tracer difference is < 1 and continues to be so over the range of Reynolds number considered. In the ocean the Reynolds number associated with a CTD package is easily $\sim 10^5 - 10^6$ and the vertical gradient in, e.g., potential temperature is likely much smaller than the value considered here. It's fair to conclude, therefore, that there would only be a very small offset between the value that a CTD would record on the downcast and that of the ambient environment. However, the same cannot be said of the upcast, which continues to exhibit large tracer differences, > 6 , across the range of Re considered.

4.3. Sensor Placement

CTD sensors are traditionally mounted at the bottom of the package and slightly off-center. However, alternative deployment locations could offer advantages, such as placing the sensor on the package's stabilizing

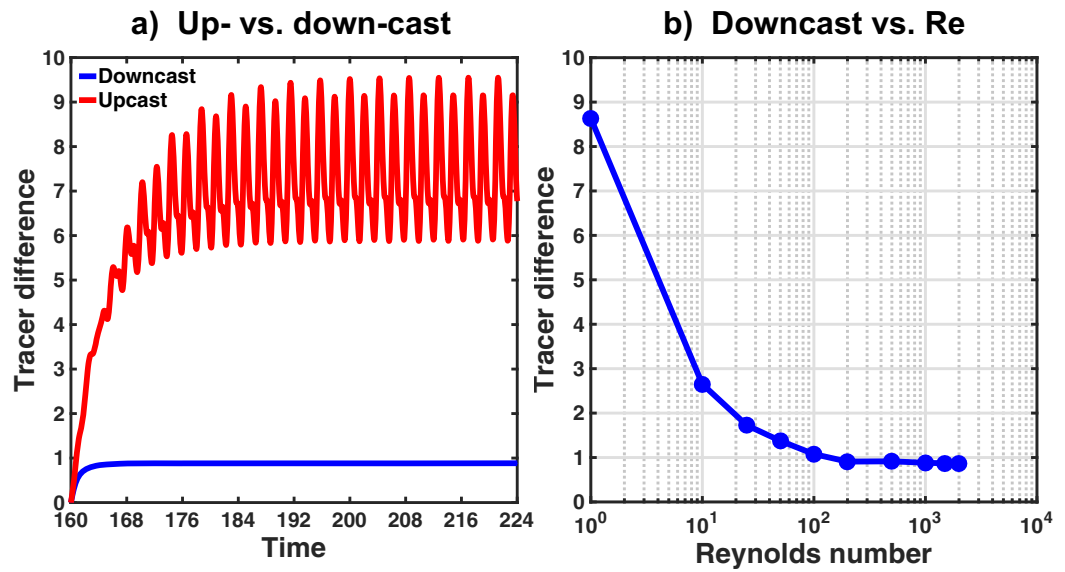


Figure 7. (a) Tracer difference on the upcast (red) and downcast (blue) sides of the cylinder at $Re=1000$ and (b) downcast tracer difference value at a range of Re .

fin. This may place the sensor in a different section of the package’s wake, which could potentially lead to less bias in the final measurement. In particular, the package will exhibit a phenomenon analogous to that of a ship’s bow wave as it descends, which may disturb the fluid on the downcast side outside of its immediate wake and boundary layers.

The effect of the cylinder’s bow wave on the upcast tracer difference is illustrated in Figure 8a for Reynolds numbers of 1 (blue) and 1000 (red). The red/blue stars mark the point at which the flow speed reaches 0.95, i.e., a location that can be considered to be outside the wake and bow wave. The thin magenta line marks where the measurement to construct Figure 7b was taken. Even at $Re=1000$, the bow wave persists for several cylinder diameters below the measurement location.

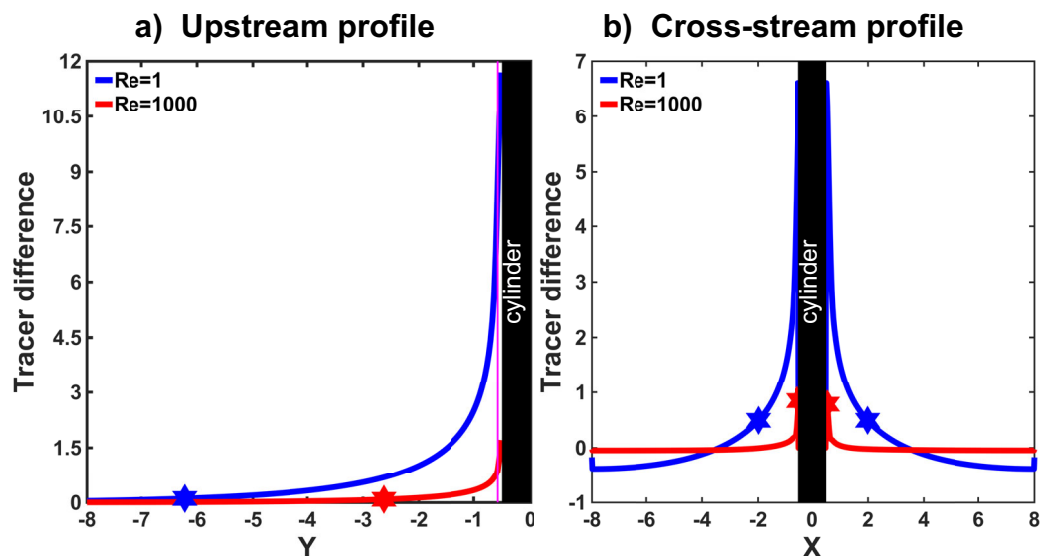


Figure 8. Profiles of tracer difference taken at the cylinder’s center line and (a) upstream of the cylinder (b) across the flow. Stars mark the point at which the upwards velocity reaches 0.95 and indicate the edge of the boundary layer and/or bow wave. The cylinder is marked in solid black and the magenta line in Figure 8a marks where the downcast side’s “measurement” is taken.

In contrast to the bow wave upstream of the cylinder, to its side, there is only a thin boundary layer. The tracer difference along the $y = 0$ axis is plotted in Figure 8b, with a star at the first location where the flow speed reaches 0.95 once more. At both $Re=1$ and $Re=1000$, the absence of a bow wave brings the location at which the free stream is attained much closer to the cylinder.

5. Oscillating Flow

As shown by Figure 3 in section 1, when the flow past a cylinder oscillates sinusoidally complex wakes and vortex interactions take place. Vortices may form on one side of the cylinder and shed on the other, implying the transport of fluid and its properties. This case has relevance to the soak stage of a CTD cast, in which the package is held below the surface to allow the sensors and pumps to equilibrate to the environment. The shedding of multiple vortices from the elements of the package could then lead to interesting anomalies in the recorded temperature/salinity values. While postprocessing will remove the soak phase from the instrument's record, the case of oscillating flow is also relevant to the collection of water samples using Niskin bottles during the upcast. During this process, the package's ascent is periodically stopped and the flow allowed to rest for ~ 30 s prior to the closing of the selected bottle.

Figure 9 shows the actual passive tracer value at $Re=1000$ and $KC=4$ and 12. The snapshot is taken eight full periods (32 and 96 time units, respectively) after initialization of the tracer. Clearly, at both values of KC the fluid are stirred by the passage of the flow past the cylinder. The shed vortices travel to both sides of the cylinder and carry fluid with them. This straining of the fluid will eventually lead to thorough mixing of the fluid. In the case of $KC=12$, there is fluid to the left of the cylinder that has traveled from below the bottom of the displayed domain and so it has a tracer value of < -8 .

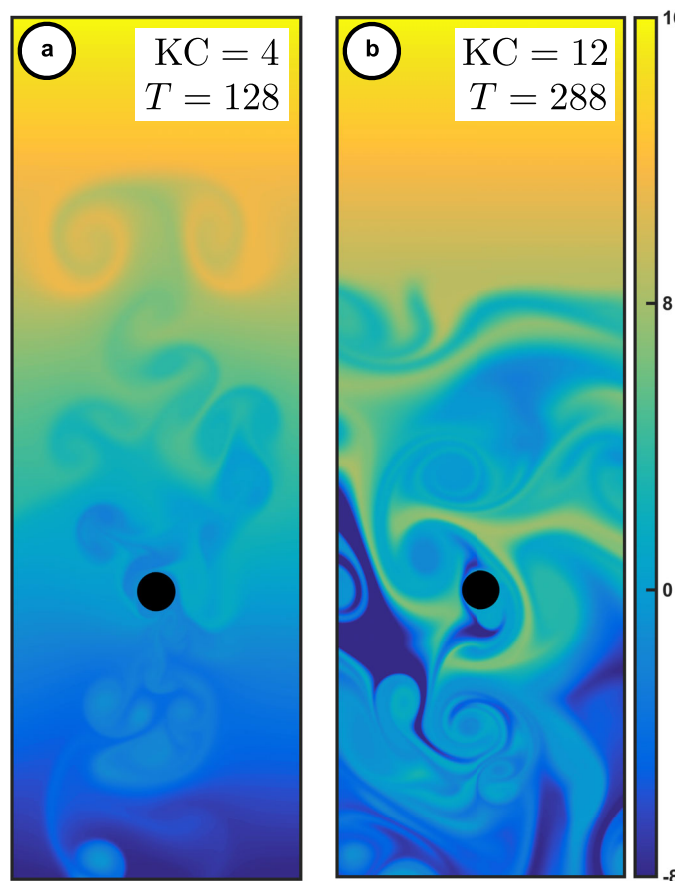


Figure 9. The actual passive tracer value at $Re=1000$ and the nondimensional time shown for (a) $KC=4$ and (b) $KC=12$. Note the suppression of variability near the top of the domain due to the presence of the sponge.

The downcast/upcast side measurements shown for both values of KC in Figure 10 show that both simulations retain the periodic nature of the oscillation. However, even during the first half cycle, the tracer difference is nonzero. Hence, the fluid in the vicinity of the measurement location is already contaminated by fluid from elsewhere. This could have important consequences for the origin depth of the water in the Niskin bottle.

6. Translation With Inline Oscillation

6.1. Different Values of KC

As reviewed in section 1 and shown in Figure 4, the combination of uniform inflow and inline oscillation can result in a complex wake and series of vortex interactions. As the ratio $\Delta U/U_0$ is increased, it is possible for the periodic oscillation to result in the flow relative to the cylinder reversing. In this case it is not just the vortex interactions with the solid walls of the cylinder that can cause them to travel to, and shed, from the downcast side of the

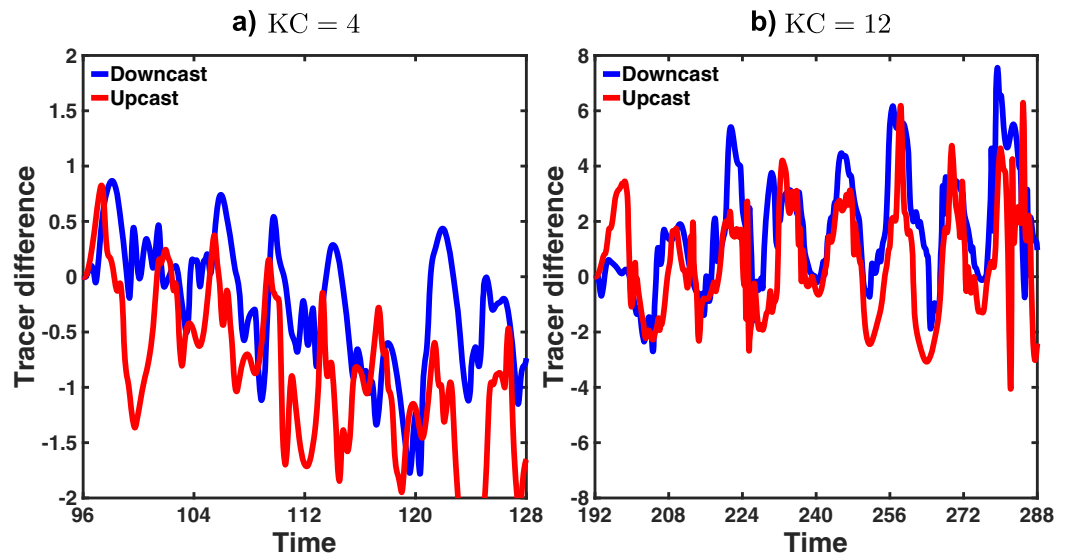


Figure 10. Tracer difference on the upcast (red) and downcast (blue) sides of the cylinder at $Re=1000$ for (a) $KC=4$ and (b) $KC=12$ over eight full cycles of the flow oscillation.

cylinder. In Figures 4e and 4f, the flow reversal helps push the newly formed vortices to the other side of the cylinder.

With three parameters controlling the flow, the Reynolds number, the Keulegan-Carpenter number/reduced velocity, and the reduced amplitude (or $\Delta U/U_0$), there are many possible regimes. The effect of an increase in KC is illustrated in Figure 11. As with the $KC=4$ simulations of Figure 4, all three of the $KC=12$ initially exhibit symmetric vortex shedding. Because of the dependence of the fluid displacement on both KC and $\Delta U/U_0$, the vortices tend to be thrown further downstream over a cycle than in Figure 4. This is most clearly seen comparing Figures 4a and 4c with Figures 11a and 11c, respectively. The detail of, e.g., the number of

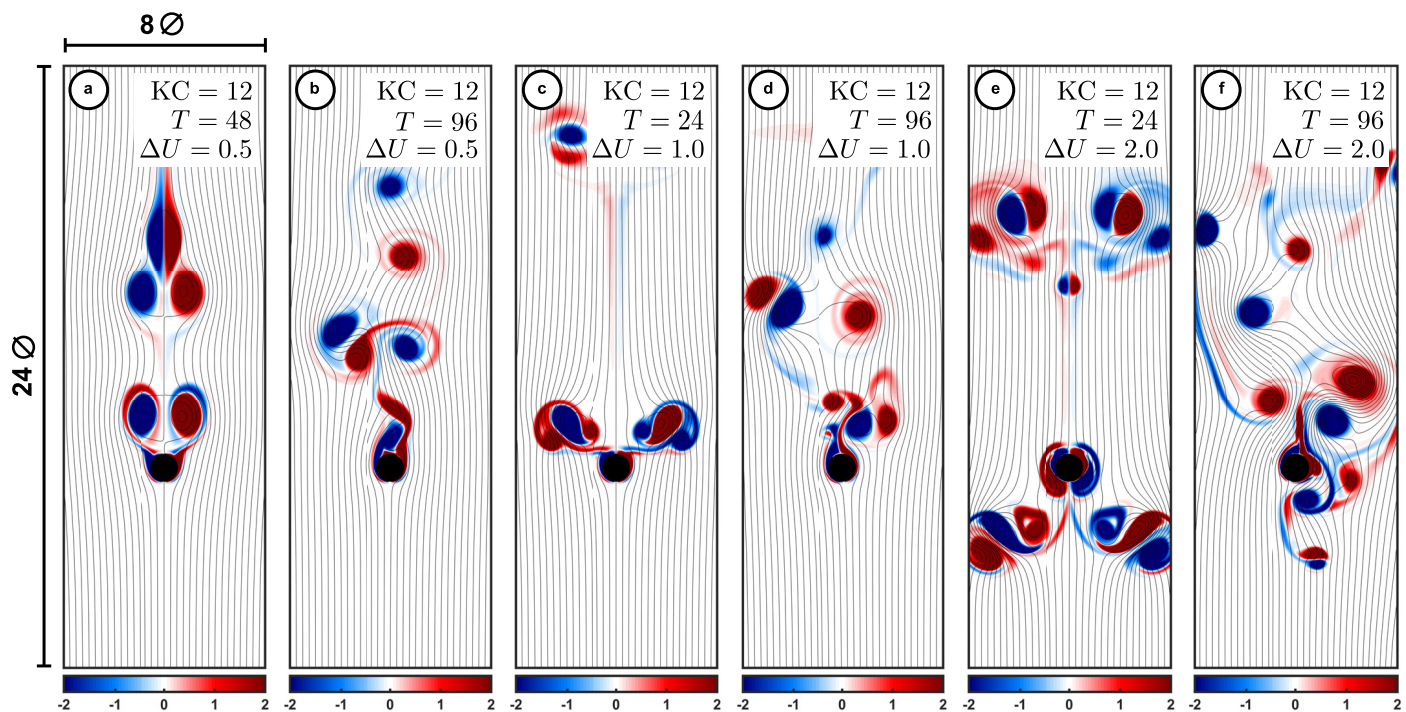


Figure 11. Numerical solutions for oscillating flow past a cylinder at the Keulegan-Carpenter number, nondimensional time, T , and ΔU shown for $Re=1000$. Each frame corresponds to the end of a full cycle and the externally imposed flow is currently at a magnitude of 1. Only part of the model domain is shown.

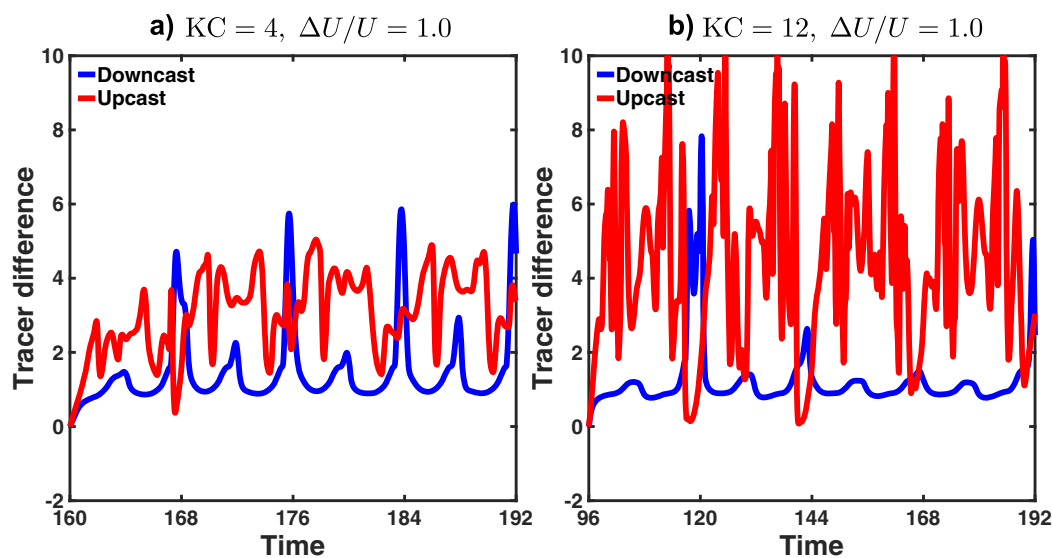


Figure 12. Tracer difference on the upcast (red) and downcast (blue) sides of the cylinder at $Re=1000$ and $\Delta U/U_0=1.0$ for (a) $KC=4$ and (b) $KC=12$ over eight full cycles of the flow oscillation.

vortices that may shed on each half cycle, etc, depends on all the parameters of the system and may change with time over an individual experiment (these phenomena can most clearly be seen in the animations of the supporting information).

6.2. Postprocessing

The longitudinal flow oscillation leads to periodic excursions of the faux tracer measurement away from the constant value attained at $Re=1000$ for a constant, uniform inflow. For both $KC=4$ and $KC=12$ (Figure 12, for $\Delta U/U_0=1.0$), the upcast measurement continues to be worse than the downcast measurement. At the longer oscillation period, the individual excursion away from the $Re=1000$ value is typically smaller. However, for both nondimensional periods, it remains possible for the downcast side measurement to be worse than the upcast. This is caused by a vortex pair shed on previous cycles of the oscillation propagating around the cylinder as the flow reverses and/or comes to a halt. This vortex pair is then pushed back into the cylinder as the flow accelerates upward once more. Another possibility is that a vortex shed on the upward half cycle may swing directly around the cylinder, as noted by *Ongoren and Rockwell* [1988] for crossflow oscillation at less than the Strouhal frequency. This can also interfere with the downcast measurement during the downward half cycle.

The variation with time of the faux tracer measurements may also be recast in terms of depth profiles by using the absolute value of the expected measurement value as “pressure.” The expected measurement is obtained by solving for the tracer value that would be at a given y and T value given the known flow and in the absence of a cylinder. In Figure 13, the blue lines have a gradient of -1 , since they are the expected value plotted against $-(\text{expected value})$. Note that for the $KC=12$ plots (Figures 13d, 13e, and 13f) the axes span a range of three times the $KC=4$ plots.

For the two simulations with the smallest $\Delta U/U_0$ of 0.5, the longitudinal oscillation is too small an amplitude for the inflow to come to rest. The resulting depth profiles of Figures 13a and 13d show a small deviation from the expected value that undergoes a periodic oscillation as the flow varies. In contrast, at $\Delta U/U_0=1.0$ and $\Delta U/U_0=2.0$, the small oscillation becomes overlaid by excursions due to the swinging of vortices around the cylinder and/or the propagation of vortices back past the cylinder. This creates tracer differences as high as 6–8 nondimensional units, as shown in Figure 12, and for the two simulations with $\Delta U/U_0=2.0$ (Figures 13c and 13f) loops begin to appear in the depth profiles. This is due to the cylinder returning to previously sampled “pressures.”

The noisy signals and loops of the depth profiles in Figure 12 and 13 are reminiscent of the same issues in the observations of Figure 1. This suggests that despite the large simplification in using a 2-D cylinder instead of a complex 3-D shape, and also the model resolution being too coarse to completely resolve the

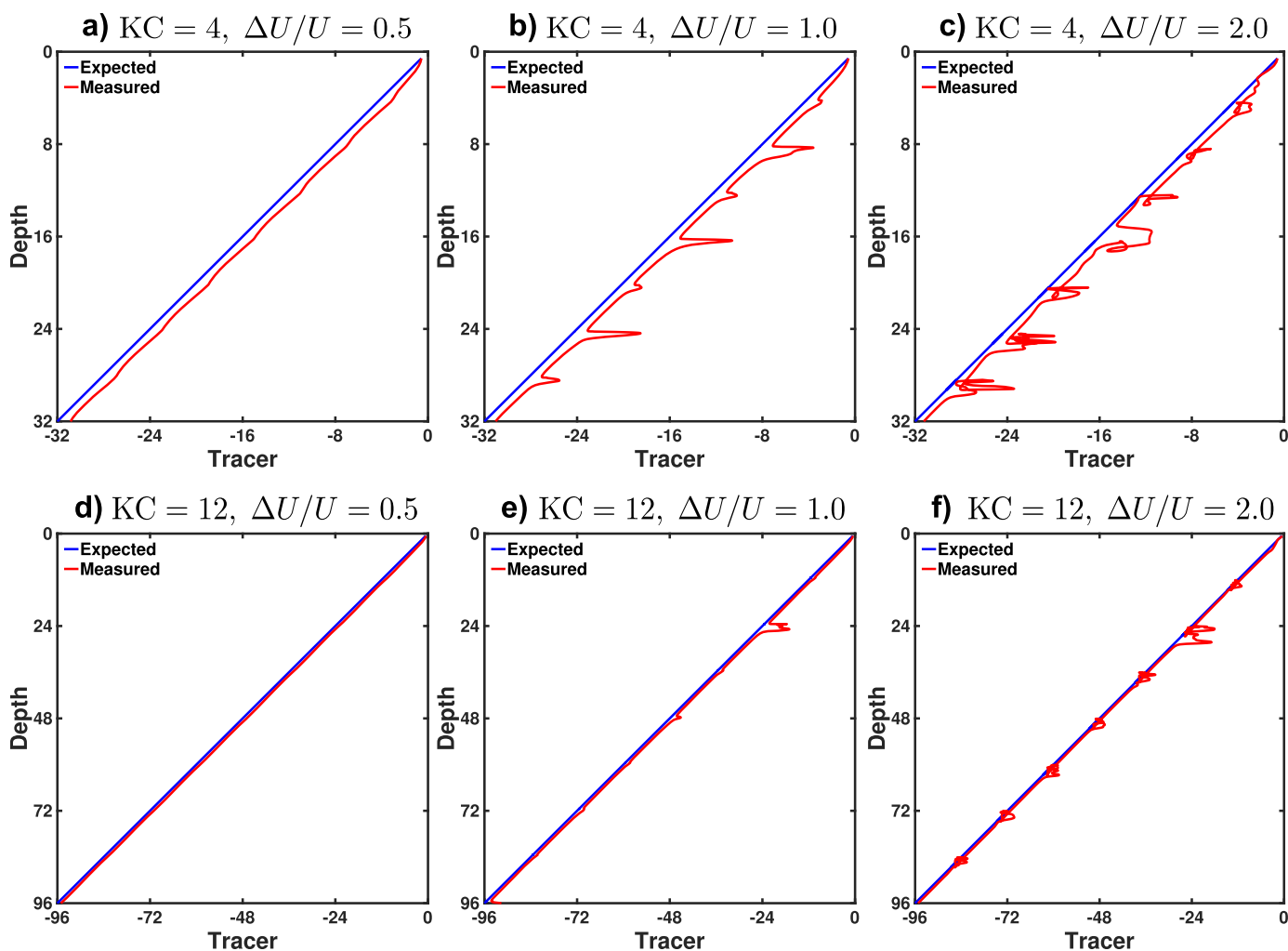


Figure 13. Unprocessed depth profiles of expected (blue) and measured (red) passive tracer values at $Re=1000$ and the KC and $\Delta U/U_0$ shown. Note the change in axes limits between $KC=4$ and $KC=12$.

boundary layer, our simulations are able to capture many of the main elements of the problem that influence the actual CTD package behavior. While important caveats remain, this indicates that our starting point of using 2-D analyses is capable of yielding some useful insights into the full complexity of the 3-D, very high Reynolds number problem.

In general, the deviations from the expected depth profile appear more egregious at $KC=4$, with apparently larger deviations. However, as highlighted in Figure 12, the tracer difference on the downcast side can be as large at $KC=12$. The apparent improvement in Figures 13e and 13f over Figures 13b and 13c largely occurs because of the axes limits. However, the increase in the period of the oscillation does allow for an overall improvement in the depth profile due to the proportional increase in the distance traveled over a full cycle from the pure translation component of the flow. This places the strong deviations from the expected tracer value farther apart in time and space and means that longer sections of the profile are less influenced by the development of the cylinder's wake.

An advantage of using a numerical modelling to investigate this problem is that the expected value is known a priori and that we have full, accurate information on the precise "depth" of the faux measurements. This means that we are able to quantitatively investigate the impact of processing procedures on the resulting depth profile, and that velocity and pressure based methods may be easily and quickly applied both together and in isolation.

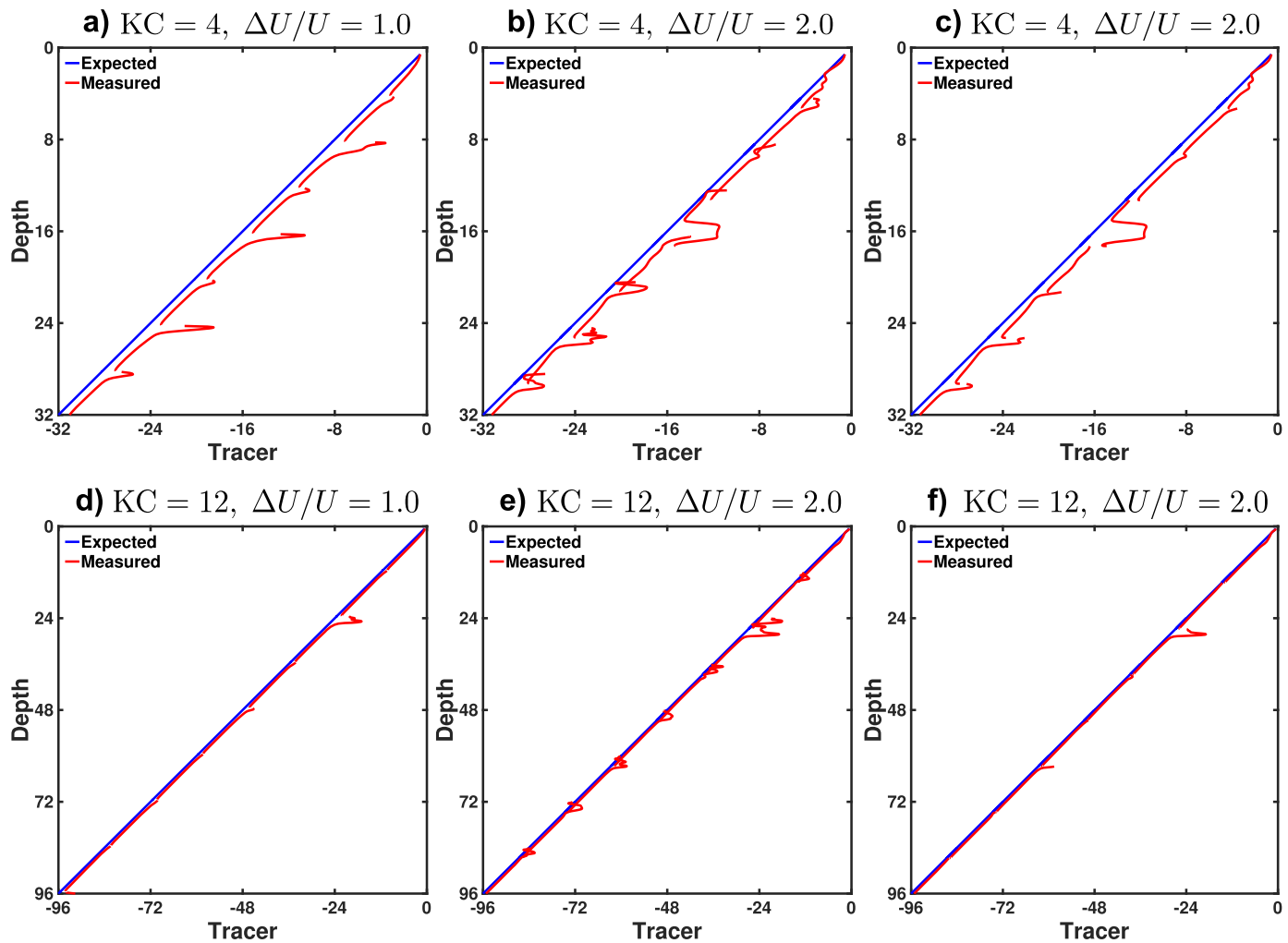


Figure 14. Processed depth profiles of expected (blue) and measured (red) passive tracer values at $Re=1000$ and the KC and $\Delta U/U_0$ shown. Note the change in axes limits between $KC=4$ and $KC=12$. (a), (b), (d), and (e) Velocity processed for $|U| < 0.25$, with (c) and (f) Pressure processed for duplicate pressure levels. Gaps in the red lines indicate where tracer values have been removed due to processing.

For the four $\Delta U/U_0=0.5$ and $\Delta U/U_0=1.0$ experiments, pressure-based processing is unable to improve the depth profiles. This is simply because the flow oscillation is not strong enough to lead to flow reversals. Velocity-based processing, in which inflow velocities of $|U| < 0.25$ are used to remove records from the depth profile, can lead to improvements by removing spikes in the tracer difference as the flow comes to rest and subsequently reaccelerates. Examples for $\Delta U/U_0=1.0$ in Figures 14a and 14d should be compared with Figures 13b and 13e, respectively. The initial departure from the expected value occurs as the flow decelerates and is eliminated by velocity processing. However, the period in which the measured value returns toward the expected value is retained in the depth profile. This is most clear in Figure 14a, for $KC=4$ and $\Delta U/U_0=1.0$. This is due to interactions between vortices with a high tracer difference and the cylinder as the flow accelerates beyond $U = 0.25$. See below for further discussion on the generation and perpetuation of these excursions.

When $\Delta U/U_0=2.0$ the flow reverses, creating loops in the depth profiles due to duplicate pressure levels (Figures 13c and 13f). Using a velocity criterion of $|U| < 0.25$ to eliminate records from the depth profile removes some of the excursions from the expected tracer value, see Figures 14b and 14e. However, the velocity criterion is exceeded before a new pressure level is reached and so some depths have more than one measured tracer value. It might be expected that the first value in time on the record would have the highest likelihood of being true to that depth. This is not always the case, due to the complex nature of the

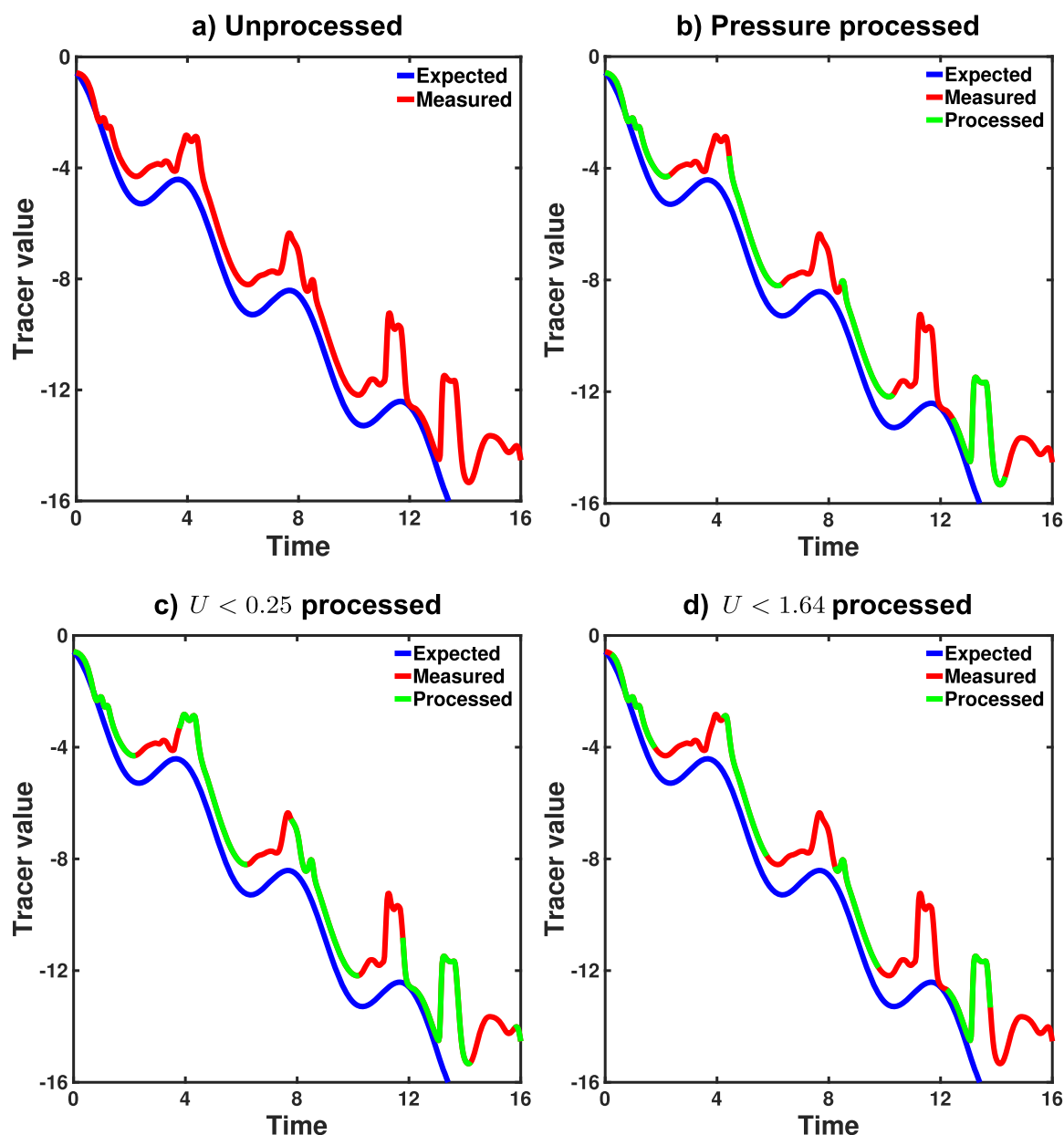


Figure 15. Variation of expected (blue) and measured passive tracer (red) with time. Values that would be retained by the processing method are marked in green.

flow-vortex-cylinder interactions, see Figure 14b at a depth of 16 units for an example. As a result, an intuitive choice for the most accurate value may sometimes lead to larger errors.

Due to the presence of duplicate pressure levels, pressure-based processing is quite successful for the two $\Delta U/U_0=2.0$ experiments. Elimination of these duplicate levels produces Figures 14c and 14f. While these Figures use breaks in the red line to indicate where processing has removed records, the profiles are continuous in depth. The pressure-based processing removes some of the excursions from the expected value that remain with solely velocity-based $|U| < 0.25$ processing. This leads to a particularly clean profile at $KC=12$. However, some of the most egregious excursions, such as that at a depth of 16 units in Figure 14c remain. While the loop beneath this excursion has been successfully removed, the large deviation itself is relatively untouched.

A clearer picture of how the different processing techniques influence the depth profile can be gained by redrawing the depth profiles as variation against time, as in Figure 15 for $KC=4$ and $\Delta U/U_0=2.0$. The

reversals of the flow are clearly visible in the expected tracer value (blue) as periodic in time returns to previously seen values. In Figures 15b–15d the measured values that would be retained using different types of postprocessing have been colored green.

Between 8 and 16 time units in Figure 15a, there is a series of three local maxima in the measured tracer that are notable as large departures from the expected value. The first of these is caused by a series of small vortices swinging around the cylinder as the flow reverses between 10 and 12 time units. These vortices carry fluid with a high tracer difference from the upcast side to the downcast side. The second peak is caused by a large and strong vortex pair that is shed from the cylinder during the flow reversal. This vortex pair translates well clear of the cylinder, with the subsequent return to upward motion forcing it directly into the cylinder's path. The third peak results from the swinging of newly formed vortices around the cylinder and interactions with the previously noted vortex pair, which leads to a complicated evolution of the flow, and tracer difference in the vicinity of the cylinder. The same three peaks are visible in Figure 13c as excursions from the expected tracer line with the central peak appearing as the blunt excursion centered at a depth of roughly 16 units and the first and third peaks being the looped sections of the measured tracer line to either side.

The application of pressure-based processing in Figure 15b successfully removes many of the local maxima, particularly the first and third of those noted above. These peaks in tracer difference occur because of the flow reversing and advecting high tracer difference fluid from the upcast side of the cylinder to the downcast side. Velocity-based processing is less successful at doing this because it does not guarantee a unique series of pressures and does not take account of the direction of travel of the fluid/cylinder. With a velocity criterion of $|U| < 0.25$ for exclusion, Figure 15c demonstrates how too few, with respect to the pressure criterion, records are removed from the depth profile. While both criteria select roughly the same start point for the exclusions (although the pressure criterion selects more precisely for $U = 0$), the velocity criterion begins to admit records to the profile before a new unique pressure is reached.

It is possible to select a velocity criterion that would only permit unique pressures in the depth profile via approximate solution of a transcendental equation. In Figure 15d this has been done by using a velocity criteria of $|U| > 1.64$. The green segments of the lines show that purely using a velocity criteria in this way is less effective than the pressure-based processing. This is because segments of the profile when the cylinder is still descending are eliminated while portions of the profile when the cylinder is still moving past its previous lowest point are retained. This tends to pollute the final profile with more bad values than the pressure-based method.

7. Summary and Discussion

Measurements taken by CTD sensors mounted on rosette frames are known to suffer from wake effects caused by the motion of the package itself. Heaving of the ship can lead to the package being pulled back up through the water column and therefore encountering pressure levels, and water, that it has previously sampled. While postprocessing of the collected data may remove some of these errors, it is difficult to do so completely.

Using the simple case of 2-D flow past a cylinder, we have performed a number of experiments that combine uniform translation with longitudinal oscillation of the flow. This problem has three controlling parameters; the Reynolds number, Re , the Keulegan-Carpenter number, KC , and the reduced amplitude A^* (or ratio of the flow oscillation to the uniform component, $\Delta U/U_0$). By using a passive tracer, it is possible to quantify the difference between the expected and actual value obtained at a specific location.

When the flow consists of purely uniform translation, the tracer difference rapidly decreases to ~ 1 for high Reynolds numbers. Potentially much smaller tracer difference could be attained by placing the sensor outside the package's frame. To place a CTD sensor outside of the bow wave would require that it dangle several meters below the base of the rosette. This could be potentially hazardous near the bottom, where swell may lead the sensor to strike the seabed, and would also be a hazard to deck crew upon deployment and retrieval of the package. Mounting the CTD sensor on the side of the frame might produce less biased measurements than one mounted at the base. If the sensor could be mounted outside of the frame, then the situation would further improve. However, such a mounting could again prove hazardous to deck crew

during deployment and retrieval, unless it could be made easily retractable, preferably remotely or autonomously. Because the rosette is affectively a permeable 3-D manifold, and CTD sensors are fitted with pumps, the actual tracer difference is likely smaller than the value we obtained for a constant fall rate.

Replacing the uniform translation of the cylinder with a purely oscillatory flow is relevant to both the soak phase of the CTD cast and the periodic stopping during the upcast to take Niskin bottle water samples. While the soak phase is removed by postprocessing, and the upcast CTD measurements are not used, the wake of the rosette could still interfere with the Niskin samples. For both long and short-period oscillation, the main action of the cylinder and its wake is to mix the part of the water column through which it moves. Because longer period oscillations lead to larger amplitude motion, this means that a larger section of the water column is being mixed. This could lead to the water sampled by the Niskin bottle coming from a different depth than intended or recorded. In this case, longer period oscillations would aggravate this source of error by potentially trapping/mixing water from further away from the intended depth.

Combining uniform translation with longitudinal oscillation of the flow generally leads to large deviations of the measured tracer value from the value expected. Longer period oscillations generally lead to an improved depth profile due to the greater distance that the cylinder moves over the course of a single cycle, rather than the errors themselves being smaller. In general this is positive; the large mass of a research vessel will effectively low pass filter the wave spectra and select for particular periods/frequencies that could reasonably be expected to tend to longer periods.

Our brief analysis of pressure-based and velocity-based postprocessing techniques indicates that the pressured-based method is very effective at removing errors due to the package being heaved back through the water column. The velocity-based techniques can potentially lead to the elimination of good data and the retention of bad. On the basis of these experiments, it is not possible to recommend a single velocity criterion that should be used for such processing. The value used is likely dependent upon the fall rate of the rosette, the particular wave environment/heave period of the ship and the shape and structure of the package itself.

The experiments here are extremely idealized. Not only is a CTD package 3-D, it is also a far more complex shape than a cylinder. We would expect this to lead to both a more complicated wake and also a smaller error on the measured tracer value. This is because while the rosette itself is large, its individual components are not, and so the boundary layers that form on them would be thin and more easily flushed. The much higher Reynolds number ($\sim 1,000,000$ compared with most of simulations of 1000) also have the potential to impact the results. In particular, such a large increase would lead to the boundary layers on the cylinder, and the entire wake, becoming turbulent. This change in behavior could lead to quantitative changes in the tracer difference that the model predicts and would require a much finer model grid and/or a change in approach to, e.g., direct numerical simulation or large eddy simulation. However, the flow through the wake and boundary layers on the cylinder would still retain fluid, as would any shed vortices. This means that the reversal of the flow and/or the passage of vortices around the cylinder or into its path could still have similar impacts to those reported here. The quantitative detail would change in critical ways, but the qualitative effects would not.

In addition to a change in Reynolds number, the next logical step toward the complexity of a real CTD package would be to extend the numerical model to simulate flow past a sphere. As with flow past a cylinder, flow past a sphere has the advantage of being governed by a single parameter, the Reynolds number and, likewise, many aesthetically compelling images are available in *Van Dyke* [1982]. However, the addition of three-dimensionality to the flow leads to some important differences. For example, at very low Reynolds number, ~ 1 , the flow past a sphere is axisymmetric and remains attached to the sphere. An increase in Re to ~ 20 – 25 leads to flow separation and the formation of an axisymmetric vortex ring on the downstream side of the sphere [see, e.g., *Taneda*, 1956; *Nakamura*, 1976]. The axisymmetry means that a 2-D plane that runs tangent to the inflow direction will appear much like the flow past a cylinder at $10 < Re < 40$ (see Figure 2b) [*Magarvey and Bishop*, 1961].

The first instability in flow past a cylinder leads to the shedding of vortices in a von Kármán vortex street and the establishment of a periodically varying wake. However, in flow past a sphere, the first symmetry breaking event is the loss of axisymmetry [*Natarajan and Acrivos*, 1993; *Tomboulides and Orszag*, 2000]. The flow remains separated, however, and no periodic vortices are shed. For a single 2-D plane, the flow will still

resemble the flow in Figure 2b. However, the orientation of this plane is essentially random, it being determined by, e.g., initialization conditions and small perturbations [see *Tomboulides and Orszag*, 2000, Figure 9]. Subsequent loss of stability does lead to the periodic shedding of vortices from the sphere. However, it takes place at considerably higher Reynolds number than for the sphere, at $Re > 290$ [Wu and Faeth, 1993; *Tomboulides and Orszag*, 2000, and references therein]. At still higher Reynolds number, the separation point/shedding point of the vortices may move around the sphere from one shedding event to the next. This can give the appearance of a helical wake, with each vortex in the train at a slightly different angle to the next. However, the vortices themselves do not spiral within the wake and instead translate away from the cylinder with their original orientation [Rodriguez et al., 2011], which is a consequence of total vorticity conservation [Achenbach, 1974].

As with flow past a cylinder, there is a highly detailed and accomplished literature regarding flow past a sphere. While these all point to a stunning array of different flow phenomena that collectively provide a wide range of beautiful flow visualizations and very different vortex behavior, one thing remains true; a three-dimensional boundary layer on an obstacle and the subsequent wake will retain fluid behind that obstacle. This means that flow reversals can still lead to a qualitatively similar behavior as seen here, i.e., that the retained fluid washes back over the obstacle and any embedded sensors leading to the sampling of characteristics from higher in the water column. While 3-D vortices will no doubt interact with each other and their generating obstacle in more complex ways than for our 2-D cylinder, there would also remain the possibility that they could directly impact the sensor measurement and/or move into the path of the package. A detailed quantitative analysis would give important information on, e.g., how vortices shed from one part of a CTD package, such as a Niskin bottle, might interact with the sensors mounted on the frame and the three-dimensionality of the system would no doubt play a key role. However, it remains likely that our central qualitative conclusions, that errors in CTD measurements can occur both because of washing of the wake directly over the sensor and the interaction of the frame with previously shed vortices, would remain true.

Acknowledgments

With thanks to the crew of the James Clark Ross during cruise JR15006. D.R.M. acknowledges interesting and insightful discussions with Hugh Venables and Ben Moat. This work was supported by the Natural Environment Research Council (ORCHESTRA, grant NE/N018095/1). The authors thank an anonymous reviewer for their comments, which led to an improvement of the paper's presentation. The model output used in this paper is available from the Open Science Framework at <https://osf.io/njmbd>.

References

- Achenbach, E. (1974), Vortex shedding from spheres, *J. Fluid Mech.*, *62*, 209–221, doi:10.1017/S0022112074000644.
- Adcroft, A., and D. Marshall (1998), How slippery are piecewise-constant coastlines in numerical ocean models?, *Tellus Ser. A*, *50*, 95–108.
- Aijun, Z. (1991), Effects of surface waves and ship heave-and-roll on CTD data and processing method for CTD data, *Chin. J. Oceanol. Limnol.*, *9*, 375–385.
- Al-Jamal, H., and C. Dalton (2013), Two-dimensional numerical simulation of a wave with a current past a circular cylinder. Part 1: Inline flow, *Appl. Math. Modell.*, *37*, 7521–7538, doi:10.1016/j.apm.2012.10.053.
- Dütsch, H., F. Durst, S. Becker, and H. Lienhart (1998), Low-Reynolds-number around an oscillating circular cylinder at low Keulegan-Carpenter numbers, *J. Fluid Mech.*, *360*, 249–271.
- Griffin, O. S., and M. S. Hall (1991), Review: Vortex shedding lock-on and flow control in bluff body wakes, *J. Fluids Eng.*, *113*, 526–537, doi:10.1115/1.2926511.
- Keulegan, G. H., and L. H. Carpenter (1958), Forces on cylinders and plates in an oscillating fluid, *J. Res. Natl Bur. Stand.*, *60*, 423–440.
- Konstantinidis, E., and S. Balabani (2007), Symmetric vortex shedding in the near wake of a circular cylinder due to streamwise perturbations, *J. Fluid Struct.*, *23*, 1047–1063, doi:10.1016/j.jfluidstruct.2007.02.002.
- Lam, K. M., and G. Q. Dai (2002), Formation of a vortex street and vortex pair from a circular cylinder oscillating in water, *Exp. Therm. Fluid Sci.*, *26*, 901–915.
- Lueck, R. G., and J. L. Picklo (1990), Thermal inertia of conductivity cells: Observations with a SeaBird cell, *J. Atmos. Oceanic Technol.*, *7*, 756–768.
- Magarvey, R. H., and R. L. Bishop (1961), Transition ranges for three-dimensional wakes, *Can. J. Phys.*, *39*, 1418–1422.
- Nakamura, I. (1976), Steady wake behind a sphere, *Phys. Fluids*, *19*, 5–8, doi:10.1063/1.861328.
- Natarajan, R., and A. Acrivos (1993), The instability of the steady flow past spheres and disks, *J. Fluid Mech.*, *254*, 323–344, doi:10.1017/S0022112093002150.
- Ongoren, A., and D. Rockwell (1988), Flow structure from an oscillating cylinder: Part I: Mechanisms of phase shift and recovery in the near wake, *J. Fluid Mech.*, *191*, 197–223, doi:10.1017/S0022112088001569.
- Rao, P. M., K. Kuwahara, and K. Tsuboi (1992), Simulation of unsteady viscous flow around a longitudinally oscillating circular cylinder in a uniform flow, *Appl. Math. Modell.*, *16*, 26–35, doi:10.1016/0307-904X(92)90112-G.
- Rodriguez, I., R. Borell, O. Lehmkuhl, C. D. Perez Segarra, and A. Oliva (2011), Direct numerical simulation of the flow over a sphere at $Re = 3700$, *J. Fluid Mech.*, *679*, 263–287, doi:10.1017/jfm.2011.136.
- Roe, P. (1985), Some contributions to the modelling of discontinuous flows, in *Large-Scale Computations in Fluid Mechanics, Lectures in Applied Mathematics*, vol. 22, edited by B. Engquist, S. Osher, and R. Somerville, pp. 163–193, Am. Math. Soc., Providence, R. I.
- Sarpkaya, T. (2005), On the parameter $\beta = Re/KC = D^2/\nu T$, *J. Fluid Struct.*, *21*, 435–440, doi:10.1016/j.jfluidstruct.2005.08.007.
- Taneda, S. (1956), Experimental investigation of the wake behind a sphere at low Reynolds numbers, *J. Phys. Soc. Jpn.*, *11*, 1104–1108, doi:10.1143/JPSJ.11.1104.
- Tansley, C. E., and D. P. Marshall (2001), Flow past a cylinder on a β plane, with application to Gulf Stream separation and the Antarctic Circumpolar Current, *J. Phys. Oceanogr.*, *31*, 3274–3283.

- Tatsuno, M., and P. W. Bearman (1990), A visual study of the flow around an oscillating circular cylinder at low Keulegan-Carpenter number and low Stokes numbers, *J. Fluid Mech.*, *211*, 157–182.
- Tomboulides, A. G., and S. A. Orszag (2000), Numerical investigation of transitional and weak turbulent flow past a sphere, *J. Fluid Mech.*, *416*, 45–74.
- Trump, C. L. (1983), Effects of ship's roll on the quality of precision CTD data, *Deep Sea Res., Part A*, *11*, 1173–1183.
- Van Dyke, M. (1982), *An Album of Fluid Motion*, 176 pp., Parabolic Press, Stanford, Calif.
- Wu, J. S., and G. M. Faeth (1993), Sphere wakes in still surrounding at intermediate Reynolds numbers, *AIAA J.*, *31*, 1448–1455.